



Spinodal decomposition enables coherent plasmonic metal/semiconductor heterostructure for full spectrum photocatalysis

Received: 22 July 2024

Accepted: 4 July 2025

Published online: 14 July 2025

Check for updates

Lisha Lu^{1,2,5}, Muhua Sun^{3,5}, Aomiao Zhi^{1,2}, Hao Ling^{1,2}, Yingying Lan⁴, Hongbo Han^{1,2}, Jianlin Wang^{1,2}, Xiaowei Zhang^{1,2}, Yu Zhao^{1,2}, Meiyun Li^{1,2}, Lejuan Cai⁴, Xiaomin Li^{1,2}, Xuedong Bai^{1,2,4} & Wenlong Wang^{1,2,4} ✉

Nanoscale metal/semiconductor heterostructures are critical components for a variety of light energy conversion applications. Herein, with plasmonic hafnium nitride (HfN) as a model system, we show that spinodal decomposition can be exploited as a unique means to produce the lattice-coherent metal/semiconductor heterostructure between HfN and its native oxynitride semiconductor—Hf₂ON₂. Atomic-resolution electron microscopy imaging provides direct visualization of the complete lattice coherency over the interface region with precisely controlled spatial modulation. The light-harvesting HfN component exhibits a broadband plasmonic absorption covering visible and near-infrared regions, and the plasmonically excited hot electrons can be efficiently injected into neighboring Hf₂ON₂ across interface. When combined with a small amount of Pt co-catalyst, the coherent HfN/Hf₂ON₂ heterostructure achieves high-efficiency photocatalytic H₂ production from methanol decomposition under visible and NIR light illumination, with apparent quantum yields of 27% at 600 nm and 13.9% at 850 nm, respectively. This performance contributes to the efficient utilization of a broad solar spectrum in photocatalysis and solar energy conversion applications.

Spinodal decomposition is an atomic level mechanism in which a thermodynamically unstable solid solution decomposes into two coexisting phases with distinctly different chemical compositions, a process that is of importance both in fundamental research and practical applications^{1–3}. Fundamental to spinodal decomposition phenomenon is the absence of an energy barrier on its transformation pathway such that the decomposition occurs through spontaneous uphill diffusion process to create nanoscale dispersed phases. As a notable consequence of this process, the two newly formed phases are

coherent with each other, showing lattice continuity at their interface^{4–6}. Spinodal decomposition phenomenon was discovered in metal alloys early in 1940's (ref. 7). In the intervening nearly a century, this mechanism has been widely explored in a lot of examples of materials where such defined phase segregation is needed so as to improve the properties and performance of materials^{4,5,8–11}. Here in this work, we present the first demonstration of the utility of spinodal decomposition as a unique means to produce the lattice coherent metal/semiconductor heterostructure for capture and conversion of

¹Beijing National Laboratory for Condensed Matter Physics, Institute of Physics, Chinese Academy of Sciences, Beijing 100190, China. ²School of Physical Sciences, University of Chinese Academy of Sciences, Beijing 100190, China. ³School of Materials Science and Engineering, Tsinghua University, Beijing 100084, China. ⁴Songshan Lake Materials Laboratory, Dongguan, Guangdong 523808, China. ⁵These authors contributed equally: Lisha Lu, Muhua Sun.

✉ e-mail: wwl@iphy.ac.cn

non-equilibrium plasmonic hot charge carriers. Such a coherent metal/semiconductor is formed between the plasmonic hafnium nitride (HfN) and its native oxynitride compound— Hf_2ON_2 , which has proven to be highly effective for directing the separation and transport of the plasmonically excited hot electrons in HfN to drive photocatalysis.

The generation of nonequilibrium hot electrons through plasmon excitation of metal nanostructures has been proposed for a wide number of applications in optical energy conversion^{12–15}. Plasmonic excitation in metal nanostructures involves the collective oscillation of surface free electrons induced by the incident radiation, offering a viable way to enhance light-matter interactions. So far, noble metals such as Ag and Au have been virtually the only materials used in plasmonic energy conversion in that the localized surface plasmon resonance (LSPR) excitation is well located in the visible and near infrared (NIR) regions^{16–18}. Known as a novel class of conductive ceramics, group IVB transition-metal nitrides (TMNs), such as titanium nitride (TiN), zirconium nitride (ZrN), and HfN show great potential as cost-effective and viable alternatives to Au and Ag. In addition to their appealing optical properties at the border of the visible and NIR regions, these nitride plasmonic materials also have more lowered work functions (ranging from 3.6 to 4.5 eV) compared to standardly used Au plasmonics, which make them more easily amenable for aligning with the electron affinity potentials of most compound semiconductors^{19,20}. Importantly, as far as the chemical nature is concerned, unlike elemental metals, TMNs are compound plasmonic materials and there exist a family of native oxide and oxynitride counterparts, which provides a basis for the rational design and construction of plasmonic metal/semiconductor heterostructures. Taken HfN for instance, its native stoichiometric oxides and oxynitrides, namely HfO_2 , $\text{Hf}_7\text{O}_8\text{N}_4$ and Hf_2ON_2 (Fig. 1a), can form a whole material family with continuously variable chemical composition and vastly different electronic band structures. Specifically, while HfN is metallic and HfO_2 is an electrical insulator with a band gap of ~ 5.1 eV (ref. 21), the in between $\text{Hf}_7\text{O}_8\text{N}_4$ and Hf_2ON_2 are both n-type semiconductors with theoretically predicted bandgaps of 3.66 eV (ref. 22) and 2.83 eV (refs. 22,23), respectively. Through a judicious combination of plasmonic HfN with its different oxides or oxynitrides, it should be possible to construct heterostructures for desired purpose.

A key challenge for the practical utilization of plasmonic hot carriers generated in metal nanostructures is their ultrashort lifetime on the order of 1 ps²⁴, which therefore requires strategies for efficiently separating hot electron-hole pairs. To this end, heterostructures consisting of plasmonic metals and appropriate semiconductors have proven to be effective, which provide a channel for quickly extracting hot carriers into the semiconductor^{13,25–27}. In general, there are two mechanisms accounting for this charge transfer process: the plasmon-induced hot electron transfer (PHET) and the plasmon-induced interfacial charge-transfer transition (PICTT)^{24,28}. The PHET mechanism involves a sequential excitation-charge transfer process of carrier generation in the metal by Landau damping, followed by transfer through tunneling or traversing the Schottky barrier. In contrast, the PICTT mechanism typically occurs in plasmonic systems with strong chemical bonds between metal nanostructures and adjacent semiconductors, where the plasmon directly damps to form separated electron-hole pairs through chemical interface damping²⁹. The PICTT alleviates the competition with hot-electron relaxation, typically showing higher efficiency and faster kinetics than PHET. In recent studies, the coexistence of both PICTT and PHET processes has been reported in several plasmonic systems, such as Au/CdSe³⁰, Ag/ TiO_2 ³¹, and Ag/CsPbBr₃³² where it significantly enhances charge transfer efficiency.

Since the efficiency of hot electrons transfer is intimately related to the nature of interface hybridization between the metal and semiconductor, it is reasonable to expect that an ideal lattice-matched, coherent interface with chemical continuity will be of intrinsic benefits

for facilitating the hot electrons transfer within a plasmonic metal/semiconductor heterostructure. The plasmonic HfN/ Hf_2ON_2 heterostructure formed via spinodal decomposition in our work is such a case in point. Crucially, both HfN and Hf_2ON_2 adopt a cubic crystal structure with relatively small lattice mismatch, which is the basis for the formation of coherent interface via spinodal decomposition. In general, spinodal decomposition is governed by the competition between local chemical free energy and composition gradient energy, such that the lattice coherency between the two newly formed phases is a natural consequence of minimizing the total energy. For a specific material system, the most direct and critical experimental criterion for assessing the occurrence of spinodal decomposition is the X-ray diffraction (XRD) characterization, as the appearance of diffraction satellite peaks and their temporal evolution directly reflect the periodic modulation of composition due to the uphill diffusion process during spinodal decomposition. For our HfN/ Hf_2ON_2 in particular, the spinodal decomposition starts from an intermediate phase with an in-between composition, and as expected, we observed the emergence of satellite sidebands, asymmetric broadening, and the progressive shift of diffraction maxima—hallmark features that are widely recognized as signatures of spinodal decomposition. Furthermore, we applied atomic-resolution scanning transmission electron microscopy (STEM) to systematically study the chemical native relationship of HfN and Hf_2ON_2 within HfN/ Hf_2ON_2 heterostructure and observed coherent interface between them. As a consequence of this structurally well-defined coherent metal/semiconductor interface, there occurs highly efficient, ultrafast hot electrons transfer from plasmonic HfN to neighboring Hf_2ON_2 , as experimentally verified by transient absorption (TA) spectroscopy measurements that show optical signatures suggesting that both PICTT and PHET pathways contribute to the interfacial electron transfer processes. For our HfN/ Hf_2ON_2 heterostructure in particular, it has a broad plasmonic absorption range, extending from visible further into NIR region, and due to the well-matched band alignment between HfN and Hf_2ON_2 the less energetic hot electrons excited by the lower energy NIR photons can be efficiently collected across the interface. These advantages of the coherent HfN/ Hf_2ON_2 heterostructure are key to enabling its practical utility for solar-to-fuel conversion applications such as photocatalysis. As a leading manifestation, we assessed the photocatalytic performance of HfN/ Hf_2ON_2 heterostructure in aqueous methanol solution for H_2 production at room temperature. When combined with a small amount of Pt co-catalyst, the coherent HfN/ Hf_2ON_2 heterostructure achieves a remarkably high rate of photocatalytic H_2 production ($14.4 \text{ mmol g}^{-1} \text{ h}^{-1}$) from methanol under visible and NIR illumination with a maximum apparent quantum yield (AQY) of 27% at 600 nm. Importantly, even with the less energetic NIR ($\lambda > 800 \text{ nm}$) photons as the only energy input, it still maintains an unexpectedly high photocatalytic activity with AQY values of 13.9% at 850 nm and 6.2% at 1064 nm. Given the prominent broadband photocatalytic activity, especially that under illumination of the less-energetic NIR photons, it offers unique possibilities for the full-spectrum solar energy utilization in photocatalysis.

Results

Figure 1b displays a simplified illustration, according to the thermodynamic description typically assumed for spinodal decomposition mechanism, of the Gibbs free energy graph and corresponding phase diagram for phase separation in the HfN- Hf_2ON_2 system. The initial and key step for producing coherent plasmonic HfN/ Hf_2ON_2 heterostructure through spinodal decomposition is to obtain an intermediate phase with a stoichiometric ratio lying between Hf_2ON_2 and HfN (Fig. 1a). In essence, such an intermediate phase, denoted as $\text{Hf}_2\text{O}_{1-x}\text{N}_2$ ($0 < x < 1$), can be regarded as a single-phase solid solution of HfN and Hf_2ON_2 , both adopting a cubic crystal structure with closely matched chemical bond lengths, which will be discussed further. Experimentally, the $\text{Hf}_2\text{O}_{1-x}\text{N}_2$ intermediate phase was synthesized by controlled

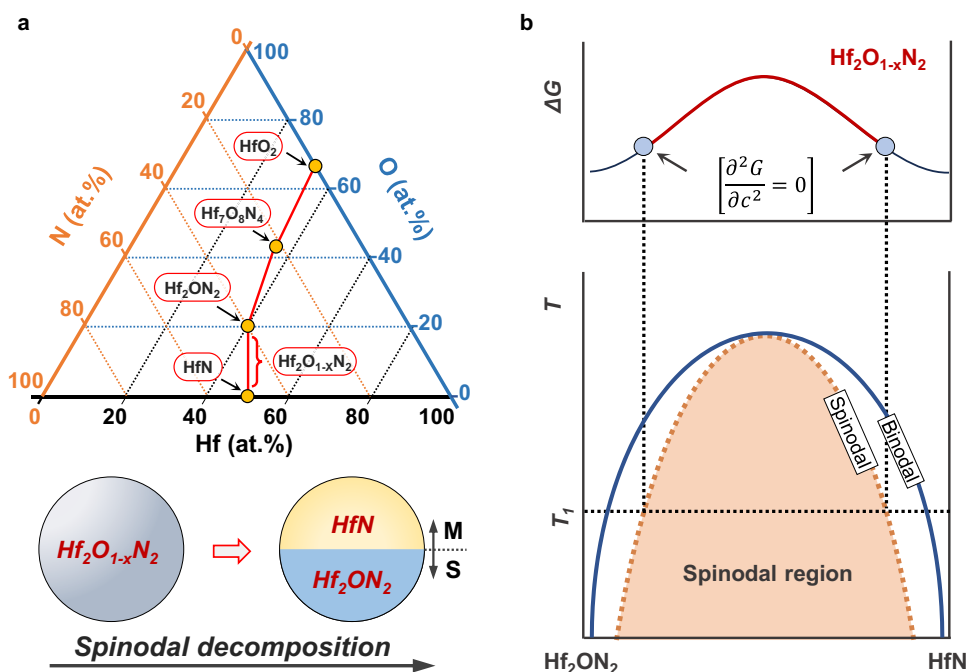


Fig. 1 | Schematic diagram of spinodal decomposition in HfN-Hf₂ON₂ system. **a** Ternary phase diagram of the Hf-O-N system. The circles filled with solid yellow denote the stoichiometric oxides and oxynitrides of Hf. They are HfO₂, Hf₇O₈N₄, Hf₂ON₂ and HfN, respectively. The non-stoichiometric oxynitrides, denoted as Hf₂O_{1-x}N₂ (0 < x < 1), vary in composition between HfN and Hf₂ON₂. The spinodal

decomposition process initiates from such Hf₂O_{1-x}N₂ intermediate phases and eventually leads to the formation of the HfN/Hf₂ON₂ heterostructure. **b** Schematic Gibbs free energy graph and the corresponding phase diagram for the HfN-Hf₂ON₂ system. The Hf₂O_{1-x}N₂ intermediate phase falls into the region of negative curvature ($\frac{\partial^2 G}{\partial c^2} < 0$), lying within the inflection points ($\frac{\partial^2 G}{\partial c^2} = 0$) of the curve.

nitridation process of HfO₂ nanoparticles using ammonia gas at elevated temperature, typically 1100 °C (see Methods for experimental details). Through the essentially similar nitridation processes, the pure-phase HfN and Hf₂ON₂ were also synthesized for structural characterization and properties assessment. As compared to pure-phase HfN and Hf₂ON₂, the controlled synthesis of the Hf₂O_{1-x}N₂ intermediate phase is intrinsically more challenging, and it is only with precise control of synthetic conditions that we can obtain the intermediate Hf₂O_{1-x}N₂ phase with varying x. With the viability of such intermediate phases, the annealing treatment at 1000 °C in an Ar atmosphere will initiate spinodal decomposition process, leading to the formation of HfN/Hf₂ON₂ heterostructures with different ratios of HfN to Hf₂ON₂; typically, the intermediate Hf₂O_{1-x}N₂ phase with larger value of x gives rise to higher volume fraction of HfN in the final heterostructure.

Synthesis and structural characterization of HfN and Hf₂ON₂

Figure 2a presents the crystal structures and local chemical environments of both HfN and Hf₂ON₂, with HfN adopting a rocksalt-type structure and Hf₂ON₂ a cubic bixbyite structure. Specifically, in crystallized HfN, each Hf atom bonds to six equivalent N atoms, forming a mixture of edge- and corner-sharing HfN₆ octahedra, while Hf₂ON₂ has a body-centered cubic structure where the Hf⁴⁺ cation is coordinated by four N and two O anions, forming a HfO₂N₄ octahedra. Powder XRD characterizations in Fig. 2b confirm that both of the as-formed HfN and Hf₂ON₂ exhibit a highly crystalline cubic structure; the HfN could be indexed to the Fm $\bar{3}$ m space group and the Hf₂ON₂ crystallized in the Ia $\bar{3}$ space group. A thorough analysis of the elemental composition of HfN and Hf₂ON₂ was conducted using inductively coupled plasma atomic emission spectroscopy (ICP-AES) and a nitrogen/oxygen elemental analyzer. The results, summarized in Supplementary Table 1, show that the elemental ratios of Hf, N, and O in all three samples closely match their ideal stoichiometric ratios. In addition, EDS mapping in Supplementary Figs. 1 and 2 demonstrates the uniformity of the element distribution.

Based on the Rietveld refined powder XRD of HfN and Hf₂ON₂ (Supplementary Fig. 3) and their structural information (Supplementary Table 3), it can be seen that the Hf-N bond length in HfN is similar to the average bond length of Hf-N and Hf-O in Hf₂ON₂. This similarity in crystal structure as well as shared chemical elements between HfN and Hf₂ON₂ suggests the possibility of forming a single-phase solid solution of Hf₂O_{1-x}N₂ intermediate phase, which serves as the starting point for spinodal decomposition. As for spinodal decomposition we are about to discuss in the next section, although this process does not involve a nucleation barrier, it is hindered by compositional gradient energy and lattice strain energy. Therefore, the more similar the structures of the final separated phases are, the lower the lattice strain energy to which spinodal decomposition is subjected when it occurs and thus the more favorable it is for decomposition to proceed. Taken together, the structural similarities of HfN and Hf₂ON₂, as well as the availability of the Hf₂O_{1-x}N₂ intermediate phase, provide a basis for the occurrence of spinodal decomposition to produce a coherent heterostructure.

Representative scanning electron microscopy (SEM) images of as-grown HfN and Hf₂ON₂ nanoparticles are shown in Supplementary Fig. 4a–d. Although the high-temperature nitridation process (above 1000 °C) inevitably induces some degree of thermal sintering, the nanoparticles largely retain their individual morphology, with an average diameter of approximately 50 nm. This morphological integrity is particularly important, as we later demonstrate that particle aggregation can significantly influence the optical response through plasmonic coupling effects. To further elucidate the atomic-scale structural features, low-magnification HAADF-STEM images and corresponding FFTs of individual HfN and Hf₂ON₂ nanoparticles along the [110] and [001] zone axes are provided in Supplementary Figs. 5a, b and 6a, b, respectively. In these HAADF-STEM images, only the Hf atomic columns are visible due to the Z-contrast, while lighter elements such as N and O are not discernible. High-resolution HAADF-STEM images taken along the [110] direction are displayed in Fig. 2c–f

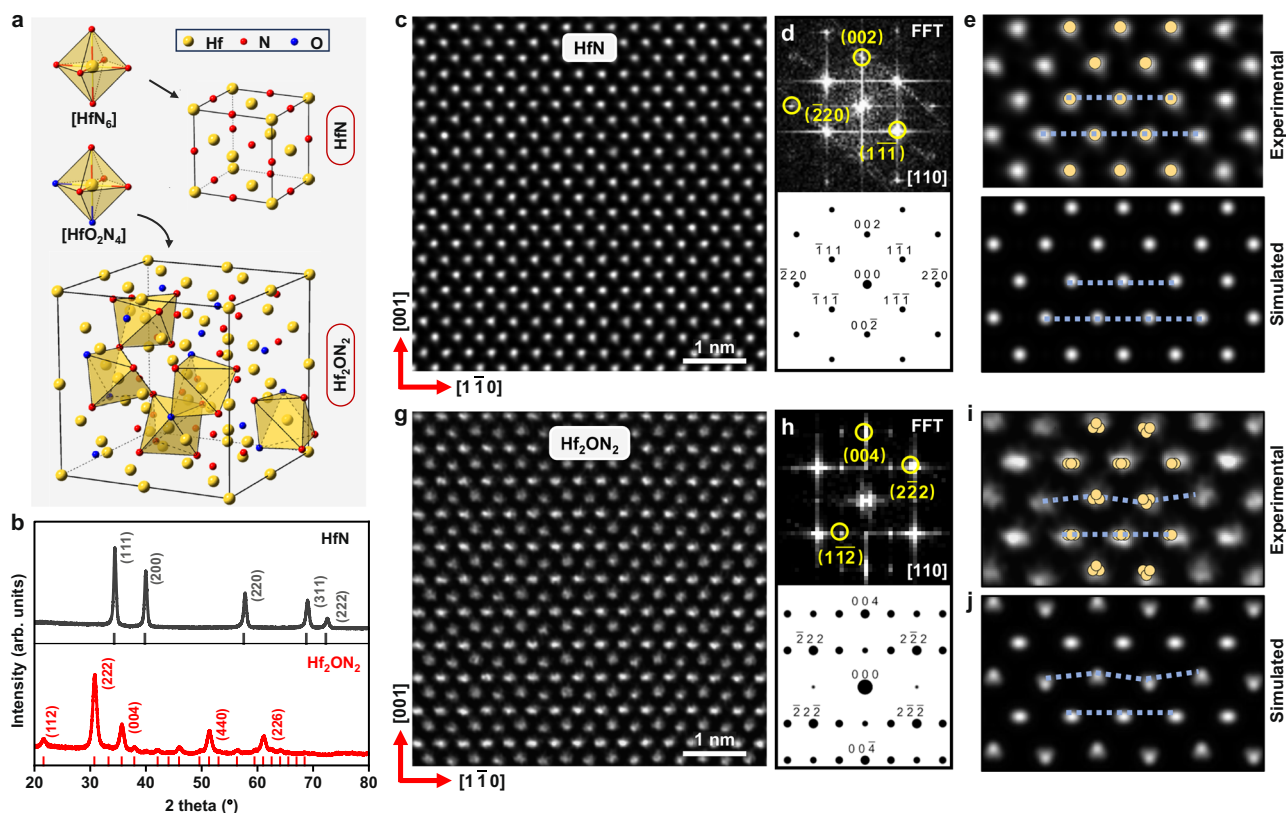


Fig. 2 | Structural characterization of HfN and Hf₂ON₂. **a, b** Crystal structures (**a**) and XRD patterns (**b**) of the single-phase HfN and Hf₂ON₂. **c, e** Atomic-resolution HAADF-STEM image of an individual HfN nanoparticle viewed along the [110] zone axis. **d** The FFT pattern (top) obtained from the HAADF-STEM image in (**c**) and the corresponding simulated electron diffraction (bottom). **e** Enlarged STEM image of (**c**) overlaid with corresponding atomic model. **f** Simulated atomic-resolution

HAADF-STEM image for comparison with (**e**). **g** Atomic-resolution HAADF-STEM image of an individual Hf₂ON₂ nanoparticle viewed along the [110] zone axis. **h** The FFT pattern (Top) and the corresponding simulated electron diffraction (bottom). **i**, Enlarged STEM image of (**g**) overlaid with atomic model. **j** The simulated atomic-resolution HAADF-STEM image corresponding to (**i**). Source data for the Fig. 2b is provided as a Source Data file.

for HfN and Fig. 2g–j for Hf₂ON₂. Despite the apparent similarity in HAADF-STEM images of HfN and Hf₂ON₂, their corresponding FFTs (Fig. 2d, h) display significantly different diffraction patterns, reflecting underlying differences in atomic structure. Specifically, an alternating shift of Hf atom positions along [110] direction is visible, as demonstrated in Fig. 2i and Supplementary Fig. 7, suggesting the presence of octahedral tilting in Hf₂ON₂. The HAADF-STEM simulations (Fig. 2f, j), obtained with imaging conditions similar to those of the experiments, reproduce the key structural features observed experimentally. These distinct FFT signatures and atomic-scale arrangements serve as reliable structural fingerprints, allowing us to clearly distinguish between HfN and Hf₂ON₂ phases.

Spinodal decomposition process and characterization of coherent interfaces

Starting from the intermediate phase Hf₂O_{1-x}N_x, spinodal decomposition takes place upon annealing at 1000 °C in an Ar atmosphere. Figure 3a shows the XRD pattern of the intermediate phase, as well as the XRD patterns of the products obtained after annealing for different durations. The magnified patterns in Fig. 3b clearly exhibit two major changes occurring during the decomposition: (1) a gradual shift of two distinct sets of diffraction peaks toward characteristic positions of the pure HfN and Hf₂ON₂ phases, respectively, and (2) the appearance of side bands adjacent to the Hf₂ON₂ (222) and HfN (200) reflections. Specifically, after 10 min of annealing, weak side bands begin to appear indicating the early stages of spinodal decomposition. These features become more pronounced at 20 min, signifying ongoing compositional modulation. By 30 min, the side bands nearly vanish, and the

primary peaks clearly resolve into two separate sets corresponding to HfN and Hf₂ON₂, indicating the completion of phase separation. The transient appearance and subsequent disappearance of these side bands reflect the onset and evolution of the periodic compositional fluctuations that are characteristic of spinodal decomposition^{33,34}. Meanwhile, the continuous shift of the main diffraction peaks suggests gradual adjustments in the average chemical composition of the evolving phases. These observations align well with well-established experimental signatures of spinodal decomposition. The essentially similar structural evolution features have been reported not only in alloy systems, but also in compound materials such as TiO₂/SnO₂^{35,36}, TiO₂/VO₂^{37,38}, TiN/AlN^{39,40} and PbS/Pb_{1-x}Sn_xTe⁴¹.

Here, it is worth noting that, for spinodal decomposition occurring at nanoscale particulate systems like our case, the nanoscale size effect also has a complex influence on this phase separation process. Specifically, the large free surfaces of nanoparticles provide a fast diffusion pathway and thereby accelerate the decomposition kinetics². Additionally, the enhanced surface energy and curvature may alter the morphological evolution during phase separation, which, in turn, affects the final biphasic textural features⁴². For ultra-small nanoparticles (e.g., <5 nm), however, the significantly elevated surface energy can thermodynamically suppress the onset of spinodal decomposition^{43,44}. In our study, the intermediate phase Hf₂O_{1-x}N_x was obtained as a nanoparticulate powder with particle sizes typically in the range of several tens of nanometers, predominantly falling within 30–70 nm (Supplementary Fig. 8a–c). At this scale, surface effects are not strong enough to suppress the spinodal decomposition process but remain appreciable to influence the decomposition kinetics. In our

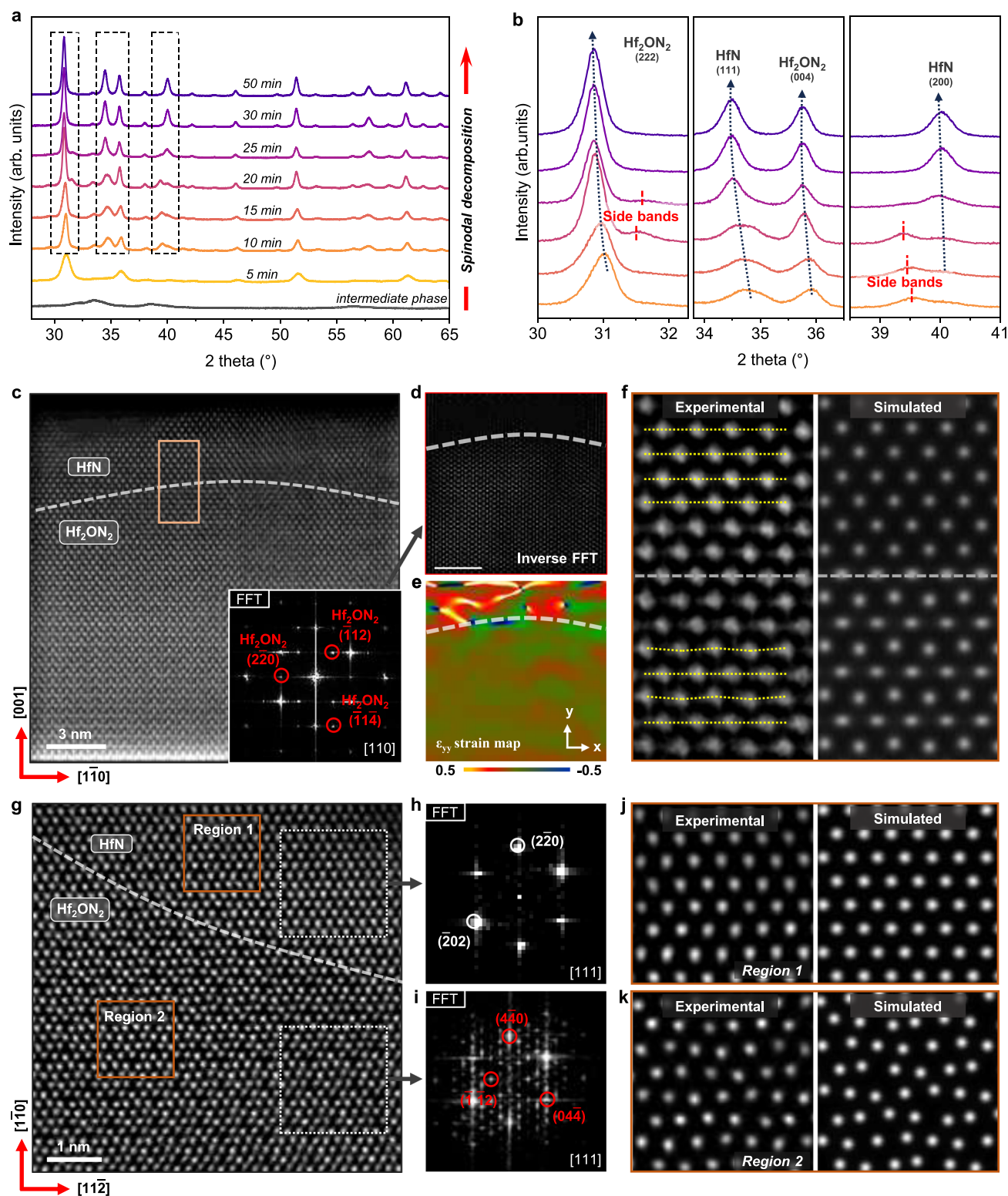


Fig. 3 | Spinodal decomposition and characterization of coherent interfaces. **a** XRD evolution during phase separation from $\text{Hf}_2\text{O}_{1-x}\text{N}_2$ intermediate phase. **b** Detailed XRD pattern showing changes in the Hf_2ON_2 (222), HfN (111), Hf_2ON_2 (004), and HfN (200) peaks. **c** HAADF-STEM image of coherent interface along [110], with composite FFT inset. **d** Inverse FFT image revealing the spatial distribution of the Hf_2ON_2 phase and interface contours, which derived from the red

solid circles representing the diffraction spots of Hf_2ON_2 . **e** GPA strain map (ϵ_{yy}) with Hf_2ON_2 as reference. **f** High-resolution STEM of HfN/ Hf_2ON_2 interface with simulated image. **g** HAADF-STEM image along the [111] zone axis. **h**, **i** FFT patterns of HfN and Hf_2ON_2 regions. **j**, **k** Enlarged STEM images of regions in (**g**) with simulated atomic-resolution images of HfN and Hf_2ON_2 , respectively. Source data for the Fig. 3a, b are provided as a Source Data file.

experiments, the entire spinodal decomposition process generally completes within 20 to 30 min, indicating rapid kinetics likely facilitated by surface effects. Moreover, such surface effects may also profoundly impact the morphological textural features of the resulting HfN/Hf₂ON₂ heterostructure, and this remains a complex issue for future investigation. The refined XRD pattern (Supplementary Fig. 9) of the final HfN/Hf₂ON₂ heterostructure shows that the ratio of HfN to Hf₂ON₂ is approximately 0.5. As mentioned earlier, the Hf₂O_{1-x}N_x intermediate phases allow for continuous and tunable adjustment of the O content by precisely controlling nitridation conditions. The XRD patterns of different intermediate phases obtained under different nitridation conditions are shown in Supplementary Fig. 10a. After the completion of spinodal decomposition, HfN/Hf₂ON₂ heterostructures with varying ratios of HfN to Hf₂ON₂ were formed. Shown in Supplementary Fig. 10b is the XRD changes during annealing process starting from another intermediate phase which was obtained at 1100 °C for 50 min. The SEM image and low-magnification STEM image in Supplementary Fig. 11 reveal the morphology of HfN/Hf₂ON₂ obtained by spinodal decomposition. It can be observed that despite undergoing high-temperature annealing, the particle size and morphology of the HfN/Hf₂ON₂ remain highly consistent with the intermediate phase prior to annealing, without further sintering or morphological changes.

The XRD characterization results presented above provide direct evidence for the occurrence of spinodal decomposition. Generally, the progression of spinodal decomposition leads to the formation of coherent or semi-coherent interfaces^{11,45,46}. In our system, both HfN and Hf₂ON₂ adopt a cubic crystal structure with a relatively small lattice mismatch, which facilitates the formation of a coherent interface during spinodal decomposition. To further substantiate this, we complemented our study with advanced HAADF-STEM characterization, which provides crucial evidence confirming the formation of lattice-coherent interfaces. Shown in Fig. 3c is a typical HAADF-STEM image of the HfN/Hf₂ON₂ heterostructure, taken along the [110] zone axis. On each side of the interface, the upper region is composed of HfN, while the lower region is Hf₂ON₂, as discerned by their respective FFT patterns (Supplementary Fig. 12a). Notably, the FFT patterns obtained from the entire field of view (Supplementary Fig. 13), including both HfN, Hf₂ON₂, and the interface, reveal nearly overlapping two sets of diffraction spots—indicative of a coherent lattice relationship between the two phases. We further employed nanobeam electron diffraction (NBED) on the heterostructure, which allows for spatially resolved diffraction from regions as small as 1–2 nm. NBED patterns collected from both sides of the interface (Supplementary Fig. 14) clearly exhibit diffraction patterns corresponding to HfN and Hf₂ON₂, respectively, confirming phase identification from the reciprocal space. Additionally, the NBED results also reveal a well-matched coherence relationship between the two phases.

To further investigate the phase distribution, we performed inverse FFT analysis by selecting diffraction spots corresponding to Hf₂ON₂ (marked with red solid circles in the inset FFT of Fig. 3c). The inverse FFT reveals the spatial distribution of Hf₂ON₂ in detail, allowing precise identification of the interface profile. To complement this, geometric phase analysis (GPA) was employed to evaluate the strain distribution across the coherent HfN/Hf₂ON₂ interface (Fig. 3e and Supplementary Fig. 15). The strain map (ϵ_{yy}) provides distinct contrast between the HfN and Hf₂ON₂ regions, thereby delineating the interface location—consistent with the boundary identified by inverse FFT analysis. The line profile of ϵ_{yy} strain map (Supplementary Fig. 15) shows that the interfacial strain is generally below 10%, a level that remains within the tolerance for coherent interface formation between HfN and Hf₂ON₂. A magnified HAADF-STEM image of the heterogeneous interface is presented in Fig. 3f, where HfN and Hf₂ON₂ domains are seen to seamlessly connect without obvious dislocations or extended defects, aligning with the corresponding locally simulated interface

region. This coherent interface forms through uphill diffusion during spinodal decomposition, driven by the minimization of interfacial energy between the emerging phases.

Further observations along the [111] zone axis (Fig. 3g) reveal distinct atomic arrangements, with corresponding FFT patterns (Fig. 3h, i) confirming the identity of HfN and Hf₂ON₂. The inverse FFT patterns in Supplementary Fig. 16c clearly delineate the position of the HfN/Hf₂ON₂ interface. Figure 3j compares the atomic arrangements in the HfN region between experimental and simulated images, while Fig. 3k presents the corresponding comparison for Hf₂ON₂, collectively confirming the formation of a coherent heterostructure. It is worth mentioning that the heterostructure along the [111] zone axis is more intuitive and easier to distinguish compared to the [110] zone axis heterostructure, due to its distinct and readily recognizable atomic arrangement. The STEM characterizations were also conducted along the [001] and [121] zone axes (Supplementary Fig. 12b, d), revealing the coherent relationship of HfN and Hf₂ON₂ along multiple crystallographic directions. Moreover, high-resolution STEM imaging combined with EELS mapping was performed along the [001] zone axis (Supplementary Figs. 16a, b and 17). The spatial distribution of N and O near the interface closely matches the heterostructure phase contrast observed in the HAADF-STEM image. Low-magnification EELS mapping (Supplementary Fig. 18) reveals an embedded heterostructure morphology consistent with the characteristic compositional modulation of spinodal decomposition. These STEM results, together with the XRD analysis of phase evolution, provide strong and complementary evidence for spinodal decomposition and the formation of the HfN/Hf₂ON₂ heterostructure with coherent interfaces. As we will discuss below, such coherent interfaces play a critical role in facilitating the extraction and transport of hot electrons from plasmonically excited HfN to semiconducting Hf₂ON₂.

Optical properties and interfacial charge transfer dynamics of HfN/Hf₂ON₂

The plasmonic properties of HfN have been extensively studied both theoretically and experimentally^{47–49}. As expected, the XPS valence-band spectrum of HfN shows a pronounced peak near the Fermi level (Supplementary Fig. 19), which is characteristic of a typical metallic electronic structure. In contrast, Hf₂ON₂ displays a typical semiconducting profile without any notable peak near the Fermi level. The metallic character of HfN and the semiconducting character of Hf₂ON₂ are further corroborated by their optical absorption spectra presented in Fig. 4a. Specifically, HfN displays broadband absorption with a peak centered around 500 nm, while Hf₂ON₂ shows typical semiconductor absorption behavior with a band edge near 480 nm, consistent with previous literature²². Upon forming the HfN/Hf₂ON₂ heterostructure, the spectrum shows both the band-edge absorption of Hf₂ON₂ and the broadband LSPR absorption of HfN, covering both the visible and NIR regions. The top panel of Fig. 4a shows the absorption spectra of HfN/Hf₂ON₂ heterostructures with varying HfN-to-Hf₂ON₂ ratios. The LSPR peaks of HfN/Hf₂ON₂ heterostructures exhibit a clear redshift and broaden further into the NIR region. Such changes in the LSPR band cannot be solely attributed to the dielectric; rather, they indicate the possible presence of strong interfacial damping between the metal and the semiconductor^{28,29}. Furthermore, the intimate contact interface and electronic interaction between HfN and Hf₂ON₂ are also evidenced by strong photoluminescence (PL) quenching, as shown in Fig. 4b. Upon selective excitation of Hf₂ON₂ with a 365 nm laser, the HfN/Hf₂ON₂ heterostructure exhibits significant photoluminescence quenching compared to pure Hf₂ON₂. This is accompanied by a decrease in PL lifetime from 4.36 ns for pure Hf₂ON₂ to 3.67 ns when coupled with HfN in the heterostructure (Fig. 4c).

As discussed above, the efficiency of plasmonic hot electron extraction in a metal/semiconductor heterostructure critically depends on the quality and extent of the contact interface. The greater

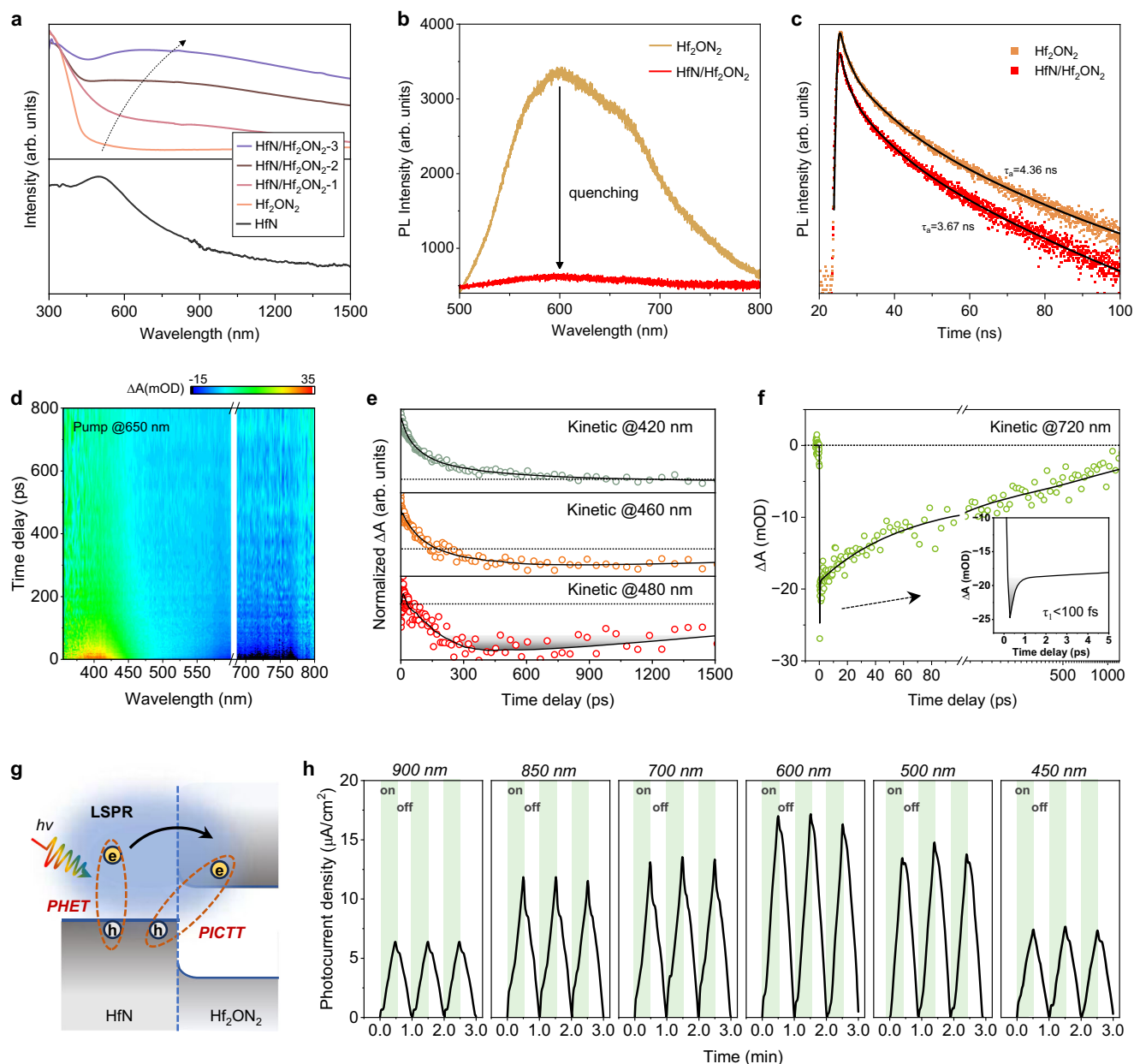


Fig. 4 | Optical properties and interfacial charge transfer dynamics of HfN/Hf₂ON₂ heterostructure. **a** UV-Vis-NIR absorption spectra of HfN/Hf₂ON₂ heterostructures with different HfN: Hf₂ON₂ ratios (1:4.5 (light red line), 1:2.1 (dark red line), 1:1.25 (pale purple line)), alongside pure-phase Hf₂ON₂ (orange) and HfN (black). **b** Steady-state PL spectra showing quenched emission in heterostructures. **c** Time resolved PL lifetime curves of HfN/Hf₂ON₂ heterostructure and the pure-phase Hf₂ON₂. **d** A two-dimensional pseudo-color plot of HfN/Hf₂ON₂

heterostructure with pump wavelength of 650 nm. **e** TA kinetics probed at different wavelengths (420 nm, 460 nm and 480 nm). **f** TA kinetics probed at 720 nm. **g** Schematic illustration of plasmon-induced hot-electron transfer in HfN/Hf₂ON₂ heterostructure after femtosecond laser pumping. **h** Transient current-time curves of HfN/Hf₂ON₂ photoanode at 0.27 V (vs Ag/AgCl) under monochromatic light irradiation. Source data for the Fig. 4a–h are provided as a Source Data file.

the extent of interface contact, the higher the electron transfer efficiency. In this work, the availability of the lattice-matched, coherent interface between the plasmonic HfN and semiconductor Hf₂ON₂ constitute the basis of highly efficient hot electrons extraction. The interfacial band structure of HfN/Hf₂ON₂ heterostructure is schematically shown in Supplementary Fig. 20. It can be seen that the interfacial barrier is small, facilitating the collection of low-energy hot electrons.

To confirm charge transfer at the metal/semiconductor interface, we employed transient absorption spectroscopy to probe the dynamics of plasmon-induced hot carriers. Figure 4d–f show the optical density change (ΔOD) spectra and time evolution of the

heterostructure samples under 650 nm optical pumping. Since the 650 nm laser has a photon energy below the band gap of Hf₂ON₂ (~480 nm), it selectively excites the LSPR of HfN within the HfN/Hf₂ON₂ heterostructure. The TA spectrum of the heterostructure is presented as a two-dimensional pseudo-color plot in Fig. 4d. The kinetic decay profile at 720 nm shown in Fig. 4f exhibits characteristics consistent with the LSPR of HfN. Apart from this dominating optical feature, crucially, at 485 nm there also rises a weak yet distinguishable bleaching signal, which corresponds to the band-edge bleaching of Hf₂ON₂. This bleaching is more clearly visible in the dynamic curve shown in Fig. 4e and Supplementary Fig. 21a, where it can be seen that the signal reaches its peak at around 300 ps and then decays. For the

pure-phase Hf_2O_3 , no transient signal is observed (Supplementary Fig. 22). Therefore, the bleaching signal at 485 nm observed in the HfN/ Hf_2O_3 heterostructure is attributed to charge transfer from HfN to Hf_2O_3 . According to the dynamics fitting at 720 nm with a multiple exponential, decay constants were obtained in Supplementary Table 4. For the HfN/ Hf_2O_3 heterostructure, an ultrafast decay component with a short lifetime (<100 fs) appears, which is absent in pure HfN (Supplementary Fig. 21b, c and Supplementary Table 4). Such an ultrafast process indicates the occurrence of PICTT with an amplitude ratio of ~30%. Furthermore, TA spectroscopy under 700 nm excitation—which efficiently excites the plasmonic resonance of HfN while minimizing spectral overlap with Hf_2O_3 —confirms the ultrafast charge transfer behavior (Supplementary Fig. 23). As we discussed earlier, PICTT requires a higher-quality interfacial contact compared to PHET, and typically both PICTT and PHET pathways contribute to the overall hot electron transfer process in plasmonic metal/semiconductor systems with strong coupling interfaces. This coexistence has been reported in several recent studies^{29–32}. The transient spectrum results present evidence of the occurrence of PICTT, evoking the picture of the coexistence of both PHET and PICTT as depicted in Fig. 4g.

Another important piece of evidence for plasmonic hot electron transfer is provided by a one-electron photoelectrochemical (PEC) model reaction. The PEC measurements were carried out in an aqueous solution containing a reversible one-electron redox couple, $[\text{Fe}(\text{CN})_6]^{3-/4-}$ (50 mM/50 mM). In these experiments, the HfN/ Hf_2O_3 heterostructure served as the photoanode, where the oxidation reaction occurred; meanwhile, photogenerated electrons generated from the photoanode were transferred to the platinum electrode via an external circuit. Electrochemical impedance spectroscopy (EIS) of the HfN/ Hf_2O_3 film shows a small semicircle in the Nyquist plot. This feature indicates an efficient charge transfer process characterized by low charge transfer resistance at the electrode–electrolyte interface (Supplementary Fig. 24a).

To corroborate the results of the transient absorption measurement, amperometric photocurrent density–time profiles (light chopping) were obtained at an applied bias voltage of 0.27 V (vs Ag/AgCl) under monochromatic light ranging from the visible to the NIR region (Fig. 4h). Under these conditions, hot electrons generated by the photoexcitation of HfN are transferred to Hf_2O_3 and then collected in the external circuit. The photocatalyst utilized to generate the photocurrent density–time profile depicted in Fig. 4h is a heterostructure with a HfN/ Hf_2O_3 ratio of 0.5. The wavelength-dependent photocurrent response measured on HfN/ Hf_2O_3 samples is shown in Supplementary Fig. 24b, together with the corresponding absorbance spectrum. The photoinduced current response qualitatively tracks the plasmonic absorbance spectra of the corresponding HfN/ Hf_2O_3 photoelectrodes, suggesting that plasmon excitation, possibly involving hot-electron generation, contributes significantly to the observed photocurrent.

Under 600 nm illumination, the photocurrent density reached 16.5 $\mu\text{A}/\text{cm}^2$. More importantly, even under NIR illumination ($\lambda > 800$ nm), the plasmonic photoanode also exhibited appreciable photocurrent responses, with photocurrent densities of 13 $\mu\text{A}/\text{cm}^2$ and 7.5 $\mu\text{A}/\text{cm}^2$ under 850 nm and 900 nm illumination, respectively. Control experiments (Supplementary Fig. 24c) with HfN alone shows decreased photocurrents under both visible and NIR illuminations compared to HfN/ Hf_2O_3 heterostructures. Hence, the enhanced photoelectrocatalytic activity of the HfN/ Hf_2O_3 heterostructure photoanode can be attributed to the lattice-coherent heterointerface, which facilitates efficient charge carrier separation and transport. Even hot electrons generated under low-energy photon excitation can transfer across the interface from HfN to Hf_2O_3 , indicating that the heterostructure possesses significant potential for full-spectrum solar energy utilization.

Photocatalytic hydrogen generation from methanol solution

To demonstrate practical utility, we employed the HfN/ Hf_2O_3 heterostructure as a photocatalyst for hydrogen production from photocatalytic methanol decomposition reaction. Following a procedure similar to those previously established^{50,51}, we investigated the H_2 evolution from aqueous methanol with the plasmonic HfN/ Hf_2O_3 heterostructure. The reaction temperature was maintained at 25 °C using a connected reflux water condenser to prevent temperature increases from light radiation, thus minimizing interference from photothermal effects. Pt was selected as the hydrogen-evolution cocatalyst and photodeposited onto the heterostructure from an aqueous H_2PtCl_6 solution. The Pt particles obtained via photodeposition exhibit a face-centered cubic crystal structure, uniform spatial distribution, and an average size of approximately 2 nm, as evidenced by Supplementary Fig. 25. Their nanometric size (~2 nm) affords a high surface area, increasing interfacial contact with the heterostructure and providing more active sites for hydrogen evolution. Given the electron flow direction in the HfN/ Hf_2O_3 system, Pt predominantly deposits on the Hf_2O_3 side, as also verified by HAADF-STEM images (Supplementary Fig. 25d).

With different amounts of Pt loading, the HfN/ Hf_2O_3 with a HfN to Hf_2O_3 ratio of 1:2.1 achieves varying degrees of improvement in hydrogen evolution (Fig. 5a). Under optical excitation, the plasmonically excited electrons from HfN can be transferred to Hf_2O_3 , and subsequently collected by Pt for initiating reaction. Specifically, in the absence of Pt, the pure HfN/ Hf_2O_3 heterostructure exhibited no observable photocatalytic activity; nevertheless, after loading a small amount of Pt, even 0.2 wt% loading, there was a noticeable boost in H_2 evolution. An optimal Pt loading of ~1.0 wt% yields an H_2 evolution rate of up to 11.2 $\text{mmol g}^{-1} \text{h}^{-1}$ under visible and NIR illumination ($\lambda > 400$ nm). With further increase of the loading amount, the rate of H_2 evolution shows no significant change. Transient absorption spectroscopy (Supplementary Fig. 26) reveals the influence of Pt loading on the carrier dynamics of both HfN and the HfN/ Hf_2O_3 heterostructure. Compared to Pt-HfN, the Pt-HfN/ Hf_2O_3 heterostructure demonstrates a longer carrier lifetime, reflecting a reduction in electron–hole recombination due to efficient electron transfer.

Under the optimal Pt loading condition, the photocatalytic activity of a series of HfN/ Hf_2O_3 heterostructures with different ratios of HfN and Hf_2O_3 were evaluated, as shown in Fig. 5b. The results reveal that the phase volume ratio of HfN to Hf_2O_3 also influences the performance of the coherent HfN/ Hf_2O_3 photocatalyst, and the best-performing ratio was found to be about 1:1.25 of HfN to Hf_2O_3 . In contrast, both bare Hf_2O_3 and HfN exhibited negligible activity for methanol decomposition, primarily due to the poor visible light absorption of Hf_2O_3 and the limited charge separation efficiency of HfN alone. This enhanced performance is attributed to the efficient transfer of plasmonically excited electrons from HfN to Hf_2O_3 under optical excitation, followed by the subsequent collection by Pt, which facilitates the hydrogen evolution reaction. Figure 5c shows the dependence of H_2 evolution on methanol concentration for the HfN/ Hf_2O_3 (1:1.25) heterostructure loaded with 1.0 wt% Pt, under visible and NIR illumination ($\lambda > 400$ nm). The H_2 evolution rate increases markedly with rising methanol concentration, with a pronounced enhancement up to 80 vol%. Even in pure methanol (100 vol%), an appreciable amount of H_2 evolution is observed, possibly indicating that the H_2 evolution is from methanol decomposition rather than water splitting, which is consistent with previously reported results in the literature^{52–54}.

The well-matched band alignment between HfN and Hf_2O_3 gives rise to a low interfacial barrier and thereby permits the collection of less-energetic hot electrons. To determine whether the less energetic photons can drive the catalytic reaction, we measured the photocatalytic activity at varied wavelengths controlled by different long-pass cut off filters, as shown in Fig. 5d. When illuminated under visible

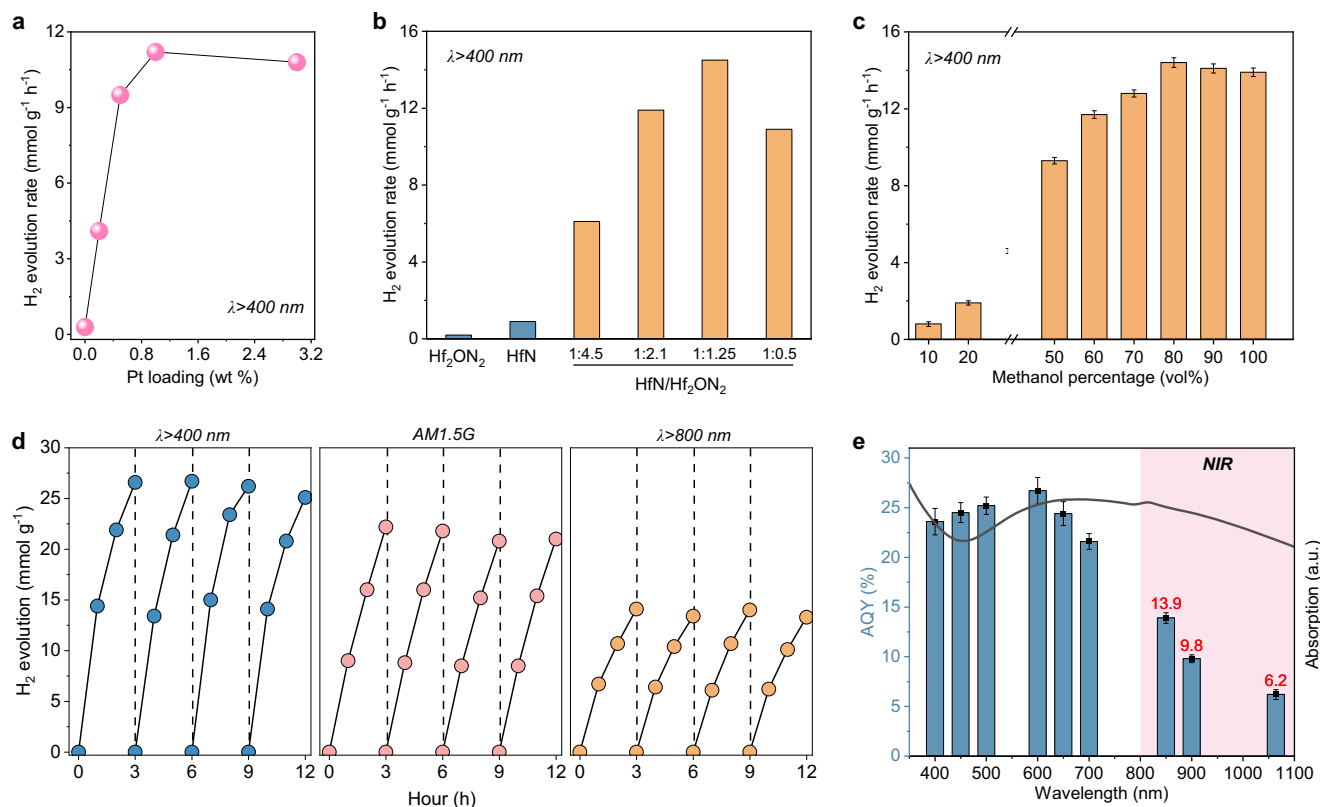


Fig. 5 | Photocatalytic H₂ generation from aqueous methanol. **a** H₂ evolution rate of Pt-HfN/Hf₂ON₂ catalysts with different amounts of Pt loading from aqueous methanol under visible and NIR light irradiation (λ > 400 nm). The ratio of HfN/Hf₂ON₂ is 1:2.1. **b** The performance for H₂ evolution of various samples with optimal Pt loading, including HfN, Hf₂ON₂, and HfN/Hf₂ON₂ heterostructures with varying ratios of HfN to Hf₂ON₂, under visible and NIR light irradiation (λ > 400 nm). **c** The effect of different methanol concentrations on H₂ evolution rates. **d** Typical time

courses of H₂ evolution amount under different illumination conditions: visible and NIR light irradiation (λ > 400 nm), AM1.5 G, and NIR light (λ > 800 nm) illumination. **e** Wavelength-dependent AQY of H₂ evolution using the Pt-HfN/Hf₂ON₂ photocatalyst, along with the UV-Vis-NIR absorption spectrum of the HfN/Hf₂ON₂ heterostructure. Error bars represent the standard deviation from three independent measurements. Source data for the Fig. 5a–e are provided as a Source Data file.

and NIR light (λ > 400 nm) for 3 h, the HfN/Hf₂ON₂ heterostructure can achieve a H₂ evolution rate of 14.4 mmol g⁻¹ h⁻¹. Remarkably, solely by NIR light illumination (λ > 800 nm), the amount of H₂ evolution still remains at a high level of 6.7 mmol g⁻¹ h⁻¹. Moreover, the HfN/Hf₂ON₂ sample presents a stable high activity over at least 12 h of reaction/evacuation processes. Figure 5e shows the wavelength-dependent AQY along with the absorbance spectrum of the HfN/Hf₂ON₂ heterostructure. The AQY closely follows the plasmonic absorbance profile, indicating that the plasmonic excitation of HfN plays a direct role in enhancing hydrogen evolution. The AQY of the HfN/Hf₂ON₂ photocatalyst exhibits a broad spectral response, with a peak value of 27% at approximately 600 nm. Importantly, even with the less energetic NIR (λ > 800 nm) photons as the only energy input, it still maintains an unexpectedly high photocatalytic activity with AQY values of 13.9% at 850 nm and 6.2% at 1064 nm. Such performance highlights the potential of the HfN/Hf₂ON₂ heterostructure for full-spectrum solar energy utilization and enhanced solar energy conversion efficiency.

For plasmonic photocatalysis, photothermal effects are also a non-negligible factor that may synergize with the hot carrier effects to drive reactions such as the methanol decomposition as investigated in our present study. Photothermal heating arises from electron-phonon scattering of unextracted hot carriers, causing localized temperature increases in plasmonic nanoparticles. Generally, the extent of this contribution varies depending on the specific reaction chemistry and operating conditions. For a nanoparticulate dispersion-based catalytic setup operated at room temperature like in our study, the efficient convective heat dissipation will limit the rise in local surface temperature^{55,56}. Such mild photothermal heating is insufficient to

drive the catalytic methanol decomposition, a reaction which, according to previous reports, requires temperatures typically above 200 °C and elevated pressures when driven purely by thermal energy. This limitation highlights the rationale behind our design of a coherent metal/semiconductor heterojunction: to enable efficient hot-electron transfer and extraction for driving the photocatalytic methanol decomposition. Indeed, as mentioned above, our transient absorption spectroscopy results provide direct evidence of efficient interfacial charge transfer from HfN to Hf₂ON₂. Importantly, further photoelectrochemical measurements confirm that the extracted hot electrons actively participate in the photochemical reactions. Therefore, it is the hot electron-driven process that plays a dominant role in the activation the photocatalytic methanol decomposition for high-efficiency H₂ generation, although the photothermal effects also synergistically contribute to the enhancements of photocatalytic rates.

Investigation of the reaction mechanism

According to previous literature^{57–59}, the reaction pathway of methanol dehydrogenation generally follows a similar mechanism under both photocatalytic and thermocatalytic conditions. The key steps involve the dissociative adsorption of methanol, the formation of intermediate species and their subsequent oxidation to produce formaldehyde (HCHO) or deeper oxidized products. To gain further insight into this process, we conducted in situ diffuse reflectance infrared Fourier transform spectroscopy (DRIFTS) to monitor methanol decomposition reaction over the Pt-HfN/Hf₂ON₂ heterostructure in liquid-phase methanol. As shown in Fig. 6a, spectra were collected over 34 min of visible light illumination, with data recorded at 1-min intervals. Before

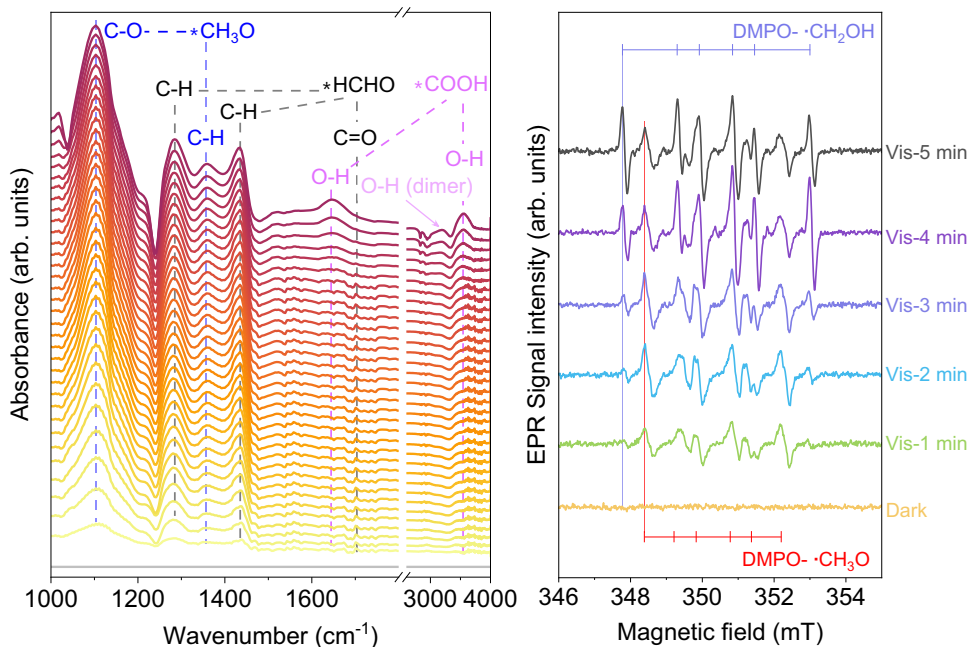


Fig. 6 | The mechanism of photocatalytic methanol decomposition. a In situ DRIFTS spectra of the Pt-HfN/Hf₂ON₂ heterostructure with and without visible light. The light gray curve represents the data obtained under dark conditions. The spectra were collected during 34 min of visible light illumination, with data

recorded at 1-min intervals. **b** DMPO adducts recorded in a pure methanol system containing Pt-HfN/Hf₂ON₂ heterostructure under ambient conditions, with and without visible-light illumination. Source data for the Fig. 6a, b are provided as a Source Data file.

illumination, the photocatalyst was immersed in methanol for 10 min to allow sufficient adsorption of methanol onto the surface.

Upon light exposure, typical infrared absorption signals of adsorbed methoxy species ($\ast\text{CH}_3\text{O}$) ($\sim 1106\text{ cm}^{-1}$, which associated with the C-O stretch vibration) appear, with their intensity increasing as the illumination time is extended. This indicates the occurrence of the dehydrogenation of CH_3OH to methoxy. The $\ast\text{CH}_3\text{O}$ species is a key intermediate during methanol decomposition. Additionally, absorption bands at ~ 1284 , 1434 , and 1703 cm^{-1} were observed, which correspond to the rocking and scissoring vibrations of C-H in adsorbed formaldehyde ($\ast\text{HCHO}$), suggesting that the reaction pathway involves the dehydrogenation of methanol to methoxy, followed by oxidation to formaldehyde and hydrogen gas. As the reaction time increases, formaldehyde undergoes further oxidation into formic acid species, evidenced by infrared absorption signals at $\sim 3542\text{ cm}^{-1}$ (O-H stretch of $\ast\text{COOH}$), 3200 cm^{-1} (O-H stretch of $\ast\text{COOH}$ dimer), and 1644 cm^{-1} (O-H bending of $\ast\text{COOH}$), signifying a deeper oxidation pathway. Furthermore, EPR spectroscopy was employed to detect radical species generated during the initial stages of the reaction. The measurements were performed in methanol solution using 5,5-dimethyl-1-pyrroline N-oxide (DMPO) as a spin-trapping agent for free radicals. As shown in Fig. 6b, two radical intermediates— $\ast\text{CH}_3\text{O}$ and hydroxymethyl ($\ast\text{CH}_2\text{OH}$)—were detected under visible light illumination. These radicals are commonly observed in methanol decomposition reactions. The combined DRIFTS data and EPR results indicate the intermediate products and the oxidation pathway are consistent with typical methanol decomposition reactions for hydrogen production.

A schematic overview of the reaction mechanism is provided in Supplementary Fig. 27. The production of electron-hole pairs in the HfN, as one of the decay channels of the surface plasmon excitation, is followed by electron transfer to the conduction band of Hf₂ON₂. These hot electrons are subsequently collected by Pt for initiating the proton reduction reaction, generating hydrogen. The remaining hot holes in HfN are directly utilized to drive the oxidation reaction of methanol, producing oxidation products such as formaldehyde and formic acid. This efficient charge separation in the HfN/Hf₂ON₂ heterostructure is

reflected in the enhanced photocatalytic hydrogen production performance.

Discussion

In plasmonic nanostructures, strong light-matter interactions enable efficient light harvesting, yet the ultrafast decay of plasmonic hot electrons often limits their direct and effective utilization in light-driven energy conversion. Devising suitable metal/semiconductor heterostructure by which to efficiently capture and separate the plasmonic hot carriers has undergone a resurgence of interest. Crucially, the extent to which the quality of interface can be achieved between plasmonic nanostructures and surrounding semiconductors will have direct influence in determining the efficiency of plasmonic hot electrons extraction and utilization. In this work, we present the first demonstration that spinodal decomposition offers a viable route to fabricate coherent metal/semiconductor heterostructures that enable highly efficient extraction of plasmonic hot electrons. By annealing a metastable Hf₂O_{1-x}N₂ intermediate phase, spontaneous phase separation occurs, leading to the formation of a HfN/Hf₂ON₂ heterostructure. Owing to their similar cubic crystal structures and small lattice mismatch, HfN and Hf₂ON₂ form atomically coherent interfaces along multiple crystallographic orientation. This plasmonic heterostructure exhibits excellent light-harvesting capability with a broadband plasmonic absorption extending from visible further to the NIR region, and in particular it also permits direct and efficient transfer of hot electrons from the optically excited HfN to semiconducting Hf₂ON₂. We present the key evidence from both TA spectroscopy and PEC measurements, demonstrating efficient charge transfer across the coherent interface between plasmonic HfN and semiconducting Hf₂ON₂ with both PICTT and PHET pathways contributing to the hot electron transfer processes.

As an important class of liquid H₂ carriers, methanol has attracted a recent resurgence of interest for its particular importance in distributed hydrogen production. To fulfill the on-demand fast H₂ release from methanol, outside the traditional methanol steam reforming approach that requires relatively high temperatures (200–350 °C) and

high pressure as well, the direct solar-driven H_2 production from photocatalytic methanol decomposition at ambient temperature has also been pursued as a more sustainable and cost-effective alternative. However, although significant advances have been made so far, the reported photocatalysts that can achieve relatively high activity are mostly limited to wide bandgap semiconductors (e.g., TiO_2) that have optical absorbance typically in the ultraviolet region. Importantly, achieving efficient full-spectrum solar-driven photocatalytic methanol decomposition requires effective light harvesting in the red and NIR regions which constitute a larger proportion of the solar spectrum. The coherent HfN/Hf₂ON₂ heterostructure reported in our present work is such a case in point. The major distinguishing features of HfN/Hf₂ON₂ heterostructure are its broadband plasmonic light harvesting and the remarkably high NIR activity for photocatalytic methanol decomposition, which provides a rational guideline for the full-spectrum solar energy utilization and photocatalysis towards high-efficiency H_2 production.

Methods

Chemicals and reagents

Hafnium chloride ($HfCl_4$, $\geq 98\%$), glucose ($C_6H_{12}O_6$, $\geq 99\%$) and urea (CH_4N_2O , $\geq 99.0\%$) were purchased from Alfa Aesar Co., Ltd. Methanol (CH_3OH , 99.9%), potassium ferricyanide ($K_3[Fe(CN)_6]$, $\geq 99.5\%$), potassium chloride (KCl, $\geq 99.99\%$), sodium sulfate (Na_2SO_4 , 99%) and deionized water were obtained from Beijing InnoChem Science & Technology Co., Ltd. Tetrapotassium Hexacyanoferrate Hydrate ($K_4[Fe(CN)_6]\cdot 3H_2O$, 98%) was purchased from Shanghai Macklin Biochemical Technology Co., Ltd. Platinum foil electrodes (Pt, $1\text{ cm} \times 1\text{ cm}$, 99.99%) and Ag/AgCl reference electrode (saturated KCl solution) were provided by Beijing Perfectlight Technology Co., Ltd. All chemicals used were of analytical grade and used without further purification.

Synthesis of HfO₂ nanosheet precursor

The HfO₂ nanosheets were synthesized using a one-pot glucose-blowing method with slight modifications to a previously reported procedure⁶⁰. In a typical experiment, 500 mg of $HfCl_4$, 5 g of glucose, and 6 g of urea were dissolved in 50 mL of deionized water under vigorous stirring. After vigorous stirring for 30 min, the homogeneous solution was heated to 140 °C for 8 h to form a porous foam. Then the mixture was calcined at 500 °C for 12 h in air to remove the glucose skeleton.

Synthesis of HfN, Hf₂ON₂ and the Hf₂O_{1-x}N₂ intermediate phase

The compounds Hf₂ON₂, HfN, and the Hf₂O_{1-x}N₂ intermediate phase were obtained starting from HfO₂ at elevated temperatures with a mixture of NH₃ and Ar flow. For pure HfN, the most vigorous reaction conditions were required: 1150 °C for 1 h with an NH₃ flow rate of 1000 mL/min and an Ar flow rate of 1000 mL/min. The reactant Hf₂ON₂ was prepared at a relatively lower temperature of 1100 °C for 30 min with an NH₃ flow rate of 500 mL/min and an Ar flow rate of 1000 mL/min. Based on the synthesis of the pure phases, the Hf₂O_{1-x}N₂ intermediate phase was obtained through a two-step synthesis method. First, HfO₂ was treated at 1100 °C for 30 min with an NH₃ flow rate of 500 mL/min and an Ar flow rate of 1000 mL/min to obtain Hf₂ON₂. Then, the NH₃ flow rate was increased to 1000 mL/min at 1100 °C for varying minutes to obtain the Hf₂O_{1-x}N₂ intermediate phase, as shown in Supplementary Fig. 10a. We note that by changing the reaction time in the second step, different intermediate phases with varying x can be obtained.

Formation of coherent HfN/Hf₂ON₂ heterostructures via spinodal decomposition

The spinodal decomposition process was initiated by annealing the Hf₂O_{1-x}N₂ intermediate phase at 1000 °C with Ar flow rate of 1000 mL/

min. Annealing for different durations yields varying degree of phase separation. Usually, the phase separation will complete at 1000 °C annealing for 50 min. Despite the high-temperature nitridation and annealing process, the samples maintained their nanosheet morphology and avoided severe particle sintering. We used a mortar and pestle to grind the samples into individual particles for subsequent characterization.

Material characterizations

XRD measurements were performed on a Rigaku diffractometer using Cu-K α irradiation, operated at 40 kV and 40 mA. SEM images were obtained using Hitachi SU8220 microscope. High-resolution Cs-corrected TEM images were acquired using a JEOL JEM-ARM300F (300 kV) equipped with a spherical aberration corrector at an accelerating voltage of 300 kV. To prepare samples for TEM imaging, nanomaterials were ultrasonically dispersed in ethanol, and a small volume of the suspension was drop-cast onto lacey carbon support films on copper grids, then air-dried before observation. UV-Vis-NIR absorption spectra were recorded using an Agilent Cary 5000 spectrophotometer. PL spectra were measured at room temperature on a Hitachi F-7000 fluorescence spectrometer with 350 nm excitation. The femtosecond TAS experiments were carried out on a Helios spectrometer, utilizing pump and probe pulses generated by a regenerative amplified Ti:sapphire laser system (Coherent, 25 fs, 4 mJ/pulse, 1 kHz repetition rate). In this work, transient absorption spectra spanning 350 to 800 nm were recorded following plasmon excitation with 650 nm or 700 nm pump pulses. Samples were prepared by dispersing finely milled powders into a PMMA solution, which was then spin-coated onto $1\text{ cm} \times 1\text{ cm}$ quartz substrate. The kinetic data for the HfN/Hf₂ON₂ heterostructure at wavelengths of 720 nm and 750 nm were analyzed using Surface Explorer software.

Diffuse reflectance infrared Fourier transform spectroscopy measurements were performed using a custom-built accessory attached to a Bruker TENSOR II spectrometer, which is equipped with a liquid-nitrogen-cooled mercury-cadmium-telluride (MCT) detector. Electron paramagnetic resonance spectra were collected at room temperature on a Bruker EPR A-300 spectrometer. Free radicals generated during formaldehyde reforming were captured at ambient conditions using DMPO as a trapping agent, followed by recording the corresponding EPR signals of these trapped radicals.

Photoelectrochemical measurements

The photocatalyst ink was prepared by grinding 2.5 mg of the powder catalyst in a mortar, followed by the addition of 50 μL Nafion solution and 5 mL methanol. The mixture was ultrasonicated for 30 min and then drop-cast onto Indium Tin Oxide (ITO) glass with a geometric area of 1 cm^2 , resulting in a catalyst loading of 2.5 mg/cm², calculated as the total catalyst mass divided by the electrode area. The coated electrode was then dried at room temperature in ambient air. Photoelectrochemical measurements were performed in a three-electrode glass cell connected to a Autolab PGSTAT 128 N Instruments. Data acquisition was performed using the Autolab PGSTAT 128 N potentiostat software. An Ag/AgCl (KCl saturated) electrode and platinum electrode were used as the reference and counter electrodes, respectively. Electrochemical impedance spectroscopy was carried out in 0.5 M Na₂SO₄ aqueous solution to evaluate the resistance of the electrochemical cell. The spectra were collected over a frequency range of 100 kHz to 0.1 Hz at open-circuit potential. The total resistance ($R_s + R_{ct}$) was extracted by fitting the Nyquist plot with an equivalent circuit model and was determined to be XX Ω .

Photocurrent-time measurements were conducted at a fixed potential of 0.27 V (vs Ag/AgCl) under chopped monochromatic light illumination. The electrolyte used was an aqueous solution containing 50 mM K₃[Fe(CN)₆], 50 mM K₄[Fe(CN)₆], and 0.5 M KCl. The electrolyte was freshly prepared before each measurement by dissolving the

reagents in deionized water and stirring until fully dissolved. It was used immediately without storage to minimize degradation, and the total volume was approximately 40 mL. The pH of the prepared solution was measured to be 7.3 ± 0.1 . For fixed wavelength of the photo-current measurement, bandpass filters with a bandwidth of less than 10 nm at the full width at half-maximum were used. All the electrochemical tests were performed at room temperature.

Photocatalytic H₂ generation from methanol solution

Pt-decorated HfN/Hf₂O₃ (Pt-HfN/Hf₂O₃) was synthesized via a commonly used photo-deposition strategy, which has been widely adopted for noble metal loading in previous studies^{61–64}. Typically, 50 mg of HfN/Hf₂O₃ nanoparticles were ultrasonically dispersed in a 100 mL H₂O/CH₃OH mixture (90 mL H₂O and 10 mL CH₃OH). Then, a measured volume of H₂PtCl₆·6H₂O solution was added under continuous stirring. The suspension was then irradiated with 365 nm UV light for 2 h at ambient temperature to photo-reduce the Pt precursor onto the nanostructure surface. After irradiation, the solid was separated by vacuum filtration, washed thoroughly with deionized water, and dried for subsequent use.

The photocatalytic hydrogen evolution reactions were conducted in a sealed gas circulation setup (MC-SPH20, Marry Change Co., Ltd). In a typical run, 50 mg of photocatalyst was dispersed in 150 mL of a methanol-water solution. Before illumination, the system was evacuated multiple times to ensure complete removal of residual air. The photocatalytic reaction was initiated by irradiating the suspension with a 300 W Xe lamp (MC-XUV300, Marry Change Co., Ltd). Light intensity was adjusted to approximately 100 mW cm⁻² ($\lambda > 400$ nm or $\lambda > 800$ nm) using a Xenon lamp or 100 mW cm⁻² under simulated sunlight (AM 1.5G). To maintain thermal stability during the reaction, the suspension temperature was controlled at 25 °C via circulating cooling water. The generated hydrogen was quantified using gas chromatography (GC) equipped with a thermal conductivity detector (TCD) and a 5 Å molecular sieve column, with argon as the carrier gas. AQY for H₂ evolution was measured under monochromatic light using band-pass filters, and calculated as follows:

$$AQY = N_e/N_p \times 100\% = 2M/N_p \times 100\%$$

where N_e is the amount of reaction electrons, N_p is the incident photons, M is the amount of H₂ molecules.

Data availability

All data supporting the findings in this paper are available within the article and its Supplementary Information. The corresponding source data files are included with the manuscript. Source data are provided with this paper.

References

- Dietl, T. et al. Spinodal nanodecomposition in semiconductors doped with transition metals. *Rev. Mod. Phys.* **87**, 1311 (2015).
- Tang, M. & Karma, A. Surface modes of coherent spinodal decomposition. *Phys. Rev. Lett.* **108**, 265701 (2012).
- Seknazi, E. et al. From spinodal decomposition to alternating layered structure within single crystals of biogenic magnesium calcite. *Nat. Commun.* **10**, 4559 (2019).
- Hou, J. X., Cao, B. X., Xiao, B., Jiao, Z. B. & Yang, T. Compositionally complex coherent precipitation-strengthened high-entropy alloys: a critical review. *Rare Met.* **41**, 2002–2015 (2022).
- Ikeda, T. et al. Self-Assembled Nanometer Lamellae of Thermoelectric PbTe and Sb₂Te₃ with Epitaxy-like Interfaces. *Chem. Mater.* **19**, 763–767 (2007).
- Park, J., Kim, G. Y., Song, K., Choi, S. Y. & Son, J. Self-assembly of correlated (Ti, V)O₂ superlattices with tunable lamella periods by kinetically enhanced spinodal decomposition. *NPG Asia Mater.* **11**, 1–9 (2019).
- DuMond, J. & Youtz, J. P. An X-ray method of determining rates of diffusion in the solid state. *J. Appl. Phys.* **11**, 357–365 (1940).
- Li, R. et al. Design of hierarchical porosity via manipulating chemical and microstructural complexities in high-entropy alloys for efficient water electrolysis. *Adv. Sci.* **9**, 2105808 (2022).
- Xiong, H. et al. A polymer-assisted spinodal decomposition strategy toward interconnected porous sodium super ionic conductor-structured polyanion-type materials and their application as a high-power sodium-ion battery cathode. *Adv. Sci.* **8**, 2004943 (2021).
- Knutsson, A., Schramm, I. C., Asp Grönhagen, K., Mücklich, F. & Odén, M. Surface directed spinodal decomposition at TiAlN/TiN interfaces. *J. Appl. Phys.* **113**, 114305 (2013).
- Rao, Z. et al. Beyond solid solution high-entropy alloys: tailoring magnetic properties via spinodal decomposition. *Adv. Funct.* **31**, 2007668 (2020).
- Naldoni, A. et al. Broadband hot-electron collection for solar water splitting with plasmonic titanium nitride. *Adv. Opt. Mater.* **5**, 1601031 (2017).
- Mubeen, S. et al. An autonomous photosynthetic device in which all charge carriers derive from surface plasmons. *Nat. Nanotechnol.* **8**, 247–251 (2013).
- Hou, B., Shen, L., Shi, H., Kapadia, R. & Cronin, S. B. Hot electron-driven photocatalytic water splitting. *PCCP* **19**, 2877–2881 (2017).
- Linic, S., Christopher, P. & Ingram, D. B. Plasmonic-metal nanostructures for efficient conversion of solar to chemical energy. *Nat. Mater.* **10**, 911–921 (2011).
- Gao, M. et al. Resonant light absorption and plasmon tunability of lateral triangular Au nanoprisms array. *Phys. Lett.* **383**, 125881 (2019).
- Liu, D. et al. Black gold: plasmonic colloidosomes with broadband absorption self-assembled from monodispersed gold nanospheres by using a reverse emulsion system. *Angew. Chem. Int. Ed. Engl.* **54**, 9596–9600 (2015).
- Chang, Q. et al. Broadband plasmonic silver nanoflowers for high-performance random lasing covering visible region. *Nanophotonics* **6**, 1151–1160 (2017).
- Patsalas, P. et al. Conductive nitrides: Growth principles, optical and electronic properties, and their perspectives in photonics and plasmonics. *Mater. Sci. Eng. R. Rep.* **123**, 1–55 (2018).
- Guler, U., Shalaev, V. M. & Boltasseva, A. Nanoparticle plasmonics: going practical with transition metal nitrides. *Mater. Today* **18**, 227–237 (2015).
- Garcia, J. C. et al. Effective masses and complex dielectric function of cubic HfO₂. *Appl. Phys. Lett.* **85**, 5022–5024 (2004).
- Thapa, B., Patterson, R. J., Conibeer, G. & Shrestha, S. Investigating electronic, optical, and phononic properties of bulk γ -M₂O₃ and β -M₇O₈N₄ (M = Hf and Zr) insulators using density functional theory. *ACS Omega* **7**, 9196–9205 (2022).
- Ino, T., Kamimuta, Y., Suzuki, M., Koyama, M. & Nishiyama, A. Dielectric constant behavior of Hf–O–N system. *Jpn. J. Appl. Phys.* **45**, 2908 (2006).
- Kale, M. J. & Christopher, P. Plasmons at the interface. *Science* **349**, 587–588 (2015).
- Ng, C. et al. Hot carrier extraction with plasmonic broadband absorbers. *ACS Nano* **10**, 4704–4711 (2016).
- DuChene, J. S., Tagliabue, G., Welch, A. J., Cheng, W.-H. & Atwater, H. A. Hot hole collection and photoelectrochemical CO₂ reduction with plasmonic Au/p-GaN photocathodes. *Nano Lett.* **18**, 2545–2550 (2018).
- Mubeen, S., Hernandez-Sosa, G., Moses, D., Lee, J. & Moskovits, M. Plasmonic photosensitization of a wide band gap semiconductor: converting plasmons to charge carriers. *Nano Lett.* **11**, 5548–5552 (2011).

28. Foerster, B. et al. Chemical interface damping depends on electrons reaching the surface. *ACS Nano* **11**, 2886–2893 (2017).
29. Wu, K., Chen, J., McBride, J. R. & Lian, T. Efficient hot-electron transfer by a plasmon-induced interfacial charge-transfer transition. *Science* **349**, 632–635 (2014).
30. Zhai, L. et al. Epitaxial growth of highly symmetrical branched noble metal-semiconductor heterostructures with efficient plasmon-induced hot-electron transfer. *Nat. Commun.* **14**, 2538 (2023).
31. Song, J. et al. Highly efficient plasmon induced hot-electron transfer at Ag/TiO₂ Interface. *ACS Photonics* **8**, 1497–1504 (2021).
32. Huang, X. et al. Efficient plasmon-hot electron conversion in Ag–CsPbBr₃ hybrid nanocrystals. *Nat. Commun.* **10**, 1163 (2019).
33. Han, K. H. On the coarsening of the modulated structure during aging of austenitic Fe–Mn–Al–C alloys prepared by the rapid solidification process. *Mater. Sci. Eng. A* **197**, 223–229 (1995).
34. Arakawa, S., Toinaga, S. & Hayashi, S. Phase separation behavior and magnetic properties of Li(Fe_xAl_{1-x})₅O₈ solid solutions. *J. Mater. Chem.* **8**, 1589 (1998).
35. Park, M., Mitchell, T. & Heuer, A. Decomposition of TiO₂–SnO₂ solid solutions. *J. Mater. Sci.* **11**, 1227–1238 (1976).
36. Yuan, T. C. & Virkar, A. V. Kinetics of spinodal decomposition in the TiO₂–SnO₂ system: the effect of aliovalent dopants. *J. Am. Ceram. Soc.* **71**, 12–21 (1988).
37. Sun, G. et al. Multi-nanolayered VO₂/Sapphire thin film via spinodal decomposition. *Sci. Rep.* **8**, 5342 (2018).
38. Chen, Z. et al. Self-assembled, nanostructured, tunable metamaterials via spinodal decomposition. *ACS Nano* **10**, 10237–10244 (2016).
39. Hu, C. et al. Self-layering of (Ti,Al)N by interface-directed spinodal decomposition of (Ti,Al)N/TiN multilayers: First-principles and experimental investigations. *Mater. Des.* **224**, 111392 (2022).
40. Bartosik, M., Rumeau, C., Hahn, R., Zhang, Z. L. & Mayrhofer, P. H. Fracture toughness and structural evolution in the TiAlN system upon annealing. *Sci. Rep.* **7**, 16476 (2017).
41. Androulakis, J. et al. Spinodal decomposition and nucleation and growth as a means to bulk nanostructured thermoelectrics: enhanced performance in Pb_{1-x}Sn_xTe–PbS. *J. Am. Chem. Soc.* **129**, 9780–9788 (2007).
42. Pankaj, P., Bhattacharyya, S. & Chatterjee, S. Surface-directed and bulk spinodal decomposition compete to decide the morphology of bimetallic nanoparticles. *Model. Simul. Mater. Sc.* **31**, 015003 (2023).
43. Radnóczy, G., Bokányi, E., Erdélyi, Z. & Misják, F. Size dependent spinodal decomposition in Cu–Ag nanoparticles. *Acta Mater.* **123**, 82–89 (2017).
44. Petsos, G. Size effects on spinodal decomposition. *Model. Simul. Mater. Sc.* **32**, 055007 (2024).
45. Chung, S. Y., Choi, S. Y., Kim, J. G. & Kim, Y. M. Quadruple-junction lattice coherency and phase separation in a binary-phase system. *Nat. Commun.* **6**, 8252 (2015).
46. Uberuaga, B., Dholabhai, P., Pilania, G. & Chen, A. Semicoherent oxide heterointerfaces: Structure, properties, and implications. *APL Mater.* **7**, 100904 (2019).
47. Askes, S. H. C., Schilder, N. J., Zoethout, E., Polman, A. & Garnett, E. C. Tunable plasmonic HfN nanoparticles and arrays. *Nanoscale* **11**, 20252–20260 (2019).
48. Singh, R., Sial, Q. A., Kim, U., Nah, S. & Seo, H. Ultrafast hot-electron injection at HfN-metal oxide heterojunctions: Role of barrier height. *Mater. Sci. Semicond. Process.* **152**, 107117 (2022).
49. O'Neill, D. B. et al. Ultrafast photoinduced heat generation by plasmonic HfN nanoparticles. *Adv. Opt. Mater.* **9**, 2100510 (2021).
50. Zhou, Y. et al. Defect engineering of metal–oxide interface for proximity of photooxidation and photoreduction. *PNAS* **116**, 10232–10237 (2019).
51. Pang, Y. et al. Colloidal single-layer photocatalysts for methanol-storable solar H₂ fuel. *Adv. Mater.* **31**, 1905540 (2019).
52. Wang, H. et al. High quantum efficiency of hydrogen production from methanol aqueous solution with PtCu–TiO₂ photocatalysts. *Nat. Mater.* **22**, 619–626 (2023).
53. Hsueh, J.-W. et al. Investigating the role of undercoordinated Pt sites at the surface of layered PtTe₂ for methanol decomposition. *Nat. Commun.* **15**, 653 (2024).
54. Miwa, T. et al. Photocatalytic hydrogen production from aqueous methanol solution with CuO/Al₂O₃/TiO₂ nanocomposite. *Int. J. Hydrog. Energy* **35**, 6554–6560 (2010).
55. Rej, S. et al. Determining plasmonic hot electrons and photothermal effects during H₂ evolution with TiN–Pt nanohybrids. *ACS Catal.* **10**, 5261–5271 (2020).
56. Kamarudheen, R., Aalbers, G. J. W., Hamans, R. F., Kamp, L. P. J. & Baldi, A. Distinguishing among all possible activation mechanisms of a plasmon-driven chemical reaction. *ACS Energy Lett.* **5**, 2605–2613 (2020).
57. Li, D. et al. NiAl₂O₄ spinel supported Pt Catalyst: high performance and origin in aqueous-phase reforming of methanol. *ACS Catal.* **9**, 9671–9682 (2019).
58. Xiao, M. et al. Unveiling the role of water in heterogeneous photocatalysis of methanol conversion for efficient hydrogen production. *Angew. Chem. Int. Ed. Engl.* **63**, e202402004 (2024).
59. Wang, X. et al. The nature of interfacial catalysis over Pt/NiAl(2)O(4) for hydrogen production from methanol reforming reaction. *J. Am. Chem. Soc.* **145**, 905–918 (2023).
60. Zhou, C. et al. Superdurable bifunctional oxygen electrocatalyst for high-performance zinc–air batteries. *J. Am. Chem. Soc.* **144**, 2694–2704 (2022).
61. Lin, L. et al. Crystalline carbon nitride semiconductors prepared at different temperatures for photocatalytic hydrogen production. *Appl. Catal. B Environ.* **231**, 234–241 (2018).
62. Lin, L. et al. Photocatalytic overall water splitting by conjugated semiconductors with crystalline poly(triazine imide) frameworks. *Chem. Sci.* **8**, 5506–5511 (2017).
63. Li, H. et al. A Na-containing Pt cocatalyst for efficient visible-light-induced hydrogen evolution on BaTaO₂N. *J. Mater. Chem. A* **9**, 13851–13854 (2021).
64. Jiang, Z. et al. Photodeposition as a facile route to tunable Pt photocatalysts for hydrogen production: on the role of methanol. *Catal. Sci. Technol.* **6**, 81–88 (2016).

Acknowledgements

This work was supported by the National Natural Science Foundation of China (22202133, 22109108, 12334001, and 51991344), the National Key R&D Program of China (2021YFA1400204), the Strategic Priority Research Program of Chinese Academy of Sciences (XDB30000000, XDB33030200), Guangdong Major Project of Basic and Applied Basic Research (2021B0301030002), Guangdong Basic and Applied Basic Research Foundation (2023A1515140102).

Author contributions

L.L. and W.W. conceived the idea and designed the experiments. W.W., X.B. and M.S. supervised the research. L.L. performed the synthesis of the samples, material characterizations, photocatalysis measurements, and data analysis. M.S. and X.L. performed the STEM measurements. A.Z. and H.H. performed the STEM images simulation. J.W. and X.Z. performed the GPA analysis. Y.L. and M.L. performed the photoelectrochemical test. H.L., Y.Z. and L.C. assisted with the discussion of the experiments. L.L., M.S., and W.W. wrote this manuscript.

Competing interests

The authors declare no competing interests.

Additional information

Supplementary information The online version contains supplementary material available at <https://doi.org/10.1038/s41467-025-61872-1>.

Correspondence and requests for materials should be addressed to Wenlong Wang.

Peer review information *Nature Communications* thanks the anonymous reviewer(s) for their contribution to the peer review of this work. A peer review file is available.

Reprints and permissions information is available at <http://www.nature.com/reprints>

Publisher's note Springer Nature remains neutral with regard to jurisdictional claims in published maps and institutional affiliations.

Open Access This article is licensed under a Creative Commons Attribution-NonCommercial-NoDerivatives 4.0 International License, which permits any non-commercial use, sharing, distribution and reproduction in any medium or format, as long as you give appropriate credit to the original author(s) and the source, provide a link to the Creative Commons licence, and indicate if you modified the licensed material. You do not have permission under this licence to share adapted material derived from this article or parts of it. The images or other third party material in this article are included in the article's Creative Commons licence, unless indicated otherwise in a credit line to the material. If material is not included in the article's Creative Commons licence and your intended use is not permitted by statutory regulation or exceeds the permitted use, you will need to obtain permission directly from the copyright holder. To view a copy of this licence, visit <http://creativecommons.org/licenses/by-nc-nd/4.0/>.

© The Author(s) 2025